Mon. Not. R. Astron. Soc. **000**, 1–10 (2015) Printed 27 October 2015 (MN LATEX style file v2.2)

Masses of the components of SB2 binaries observed with *Gaia*. II. Masses derived from *PIONIER* interferometric observations for *Gaia* validation ⋆⋆ †† ‡‡

arXiv:1510.07412v1 [astro-ph.SR] 26 Oct 2015

J.-L. Halbwachs[1]§, H.M.J. Boffin[2], J.-B. Le Bouquin[3], F. Kiefer[4], B. Famaey[1], J.-B. Salomon[1], F. Arenou[5], D. Pourbaix[6,7], F. Anthonioz[3], R. Grellmann[8], S. Guieu[3], H. Sana[9], P. Guillout[1], A. Jorissen[7], Y. Lebreton[5,10], T. Mazeh[4], L. Tal-Or[4,11] and A. Nebot Gómez-Morán[1]

[1] *Observatoire astronomique de Strasbourg, Université de Strasbourg, CNRS, UMR 7550, 11 rue de l'Université, 67000 Strasbourg, France*
[2] *ESO, Av. Alonso de Cordova 3107, 19001 Casilla, Santiago 19, Chile*
[3] *UJF-Grenoble 1/CNRS-INSU, UMR 5274, Institut de Planétologie et d'Astrophysique de Grenoble (IPAG), 38041 Grenoble, France*
[4] *School of Physics and Astronomy, Tel Aviv University, Tel Aviv 69978, Israel*
[5] *GEPI, Observatoire de Paris, CNRS, Université Paris Diderot, 5 place Jules Janssen, 92195, Meudon, France*
[6] *F.R.S.-FNRS, Rue d'Egmont 5, 1000 Bruxelles, Belgium*
[7] *Institut d'Astronomie et d'Astrophysique, Université Libre de Bruxelles, boulevard du Triomphe, 1050 Bruxelles, Belgium*
[8] *Physikalisches Institut der Universität zu Köln, Zülpicher Strasse 77, D-50937 Köln, Germany*
[9] *Institute of Astronomy, KU Leuven, Celestijnenlaan 200D, 3001 Leuven, Belgium*
[10] *Institut de Physique de Rennes, Université de Rennes 1, CNRS UMR 6251, 35042 Rennes, France*
[11] *Institut für Astrophysik (IAG), Friedrich-Hund-Platz 1, D-37077 Göttingen, Germany*

Accepted 2015 October 23. Received 2015 October 20; in original form 2015 September 30

ABSTRACT

In anticipation of the *Gaia* astrometric mission, a sample of spectroscopic binaries is being observed since 2010 with the *Sophie* spectrograph at the Haute–Provence Observatory. Our aim is to derive the orbital elements of double-lined spectroscopic binaries (SB2s) with an accuracy sufficient to finally obtain the masses of the components with relative errors as small as 1 % when combined with *Gaia* astrometric measurements. In order to validate the masses derived from *Gaia*, interferometric observations are obtained for three SB2s in our sample with F-K components: HIP 14157, HIP 20601 and HIP 117186. The masses of the six stellar components are derived. Due to its edge-on orientation, HIP 14157 is probably an eclipsing binary. We note that almost all the derived masses are a few percent larger than the expectations from the standard spectral-type-mass calibration and mass-luminosity relation. Our calculation also leads to accurate parallaxes for the three binaries, and the *Hipparcos* parallaxes are confirmed.

Key words: binaries: spectroscopic, binaries: visual, stars: fundamental parameters, stars: individual:HIP 14157, HIP 20601, HIP 117186

1 INTRODUCTION

In a previous paper (Halbwachs et al. 2014), we presented the selection of a sample of double-lined spectroscopic binaries (SB2) for which it will be possible to derive accurately the masses of the components when the astrometric measurements of the *Gaia* satellite will be delivered. Our aim is to obtain high-precision radial velocity (RV) measurements in order to derive the minimum masses of the components, $\mathcal{M}_1 \sin^3 i$ and $\mathcal{M}_2 \sin^3 i$, where $\mathcal{M}_1$ and $\mathcal{M}_2$ are the masses and i is the inclination of the orbital plane on the plane of the sky. The *Gaia* astrometric measurements of

⋆ based on observations performed at the Observatoire de Haute–Provence (CNRS), France
† based on observations performed with the *HERMES* spectrograph at the Roque de los Muchachos Observatory
‡ based on data obtained with the ESO Very Large Telescope under programme 094.D-0624, 094.C-0884, 094.C-0175 and 094.C-0397.
§ E-mail: jean-louis.halbwachs@astro.unistra.fr

© 2015 RAS

the photocentre of these systems will lead to the derivation of astrometric orbits, including i, and therefore to $\mathcal{M}_1$ and $\mathcal{M}_2$. The RV measurements are obtained through two different programs: a programme of about 70 SB2 is carried on with the T193 telescope of the Haute-Provence observatory (*OHP*) with the *Sophie* spectrograph, and a separate programme of seven SB2 is using the Mercator 1.2m–telescope at the Roque de los Muchachos Observatory (*RMO*), with the *HERMES* spectrograph (Raskin et al. 2011).

Despite the high quality that is expected for the *Gaia* measurements, we know from the reduction of the *Hipparcos* satellite (ESA 1997; van Leeuwen 2007) that large space astrometric surveys may be prone to systematic errors. The discussion about the reliability of the *Hipparcos* results is still not closed: recently, Fekel (2015) found an important discrepancy between the parallax he obtained for the system HD 207651, and the parallax given in the *Hipparcos 2* catalogue (van Leeuwen 2007), even when the orbital motion is taken into account.

The large variations affecting the basic angle of *Gaia* will make the verification of the *Gaia* measurements even more necessary (Mora et al. 2015). Regarding double stars, a good orbit determination with *Gaia* depends on the measurements at various epochs, and ultimately rely on the application of the Point Spread Function (PSF) calibration, considering the object as a single star. Binaries may then be sensitive to small differences between the position given by the PSF and the position of the actual photocentre. Therefore, an independent derivation of the masses of some stars of our sample is welcome in order to validate our future results.

For these reasons, we obtained interferometric measurements with the *PIONIER* instrument at the Very Large Telescope Interferometer (*VLTI*). After one semester, three SB2s were observed over nearly half of their period. Two of these systems are from the *OHP* programme, and the other is from the *RMO* programme. HIP 14157 is a couple of chromospherically active K-dwarf stars which was noticed by Fekel, Henry & Alston (2004) for their large minimum masses. HIP 20601 is a Hyades binary star observed by Griffin et al. (1985), and that seems also to have components with masses above expectations. HIP 117186 is an early F-type dwarf from the sample of Nordström et al. (1997).

The obtention of the interferometric observations is described in section 2. The RV data and the calculation of the SB2 orbital elements are in section 3. The masses of the six components are derived hereafter, in section 4. Our results are used to derive the mass-luminosity relation in the infrared H band, in section 5, and also to verify the *Hipparcos* parallaxes, in section 6. We conclude in section 7.

2 THE INTERFEROMETRIC OBSERVATIONS

2.1 The observations

We observed our three systems with the four 1.8-m Auxiliary Telescopes of *ESO* Very Large Telescope Interferometer, using the *PIONIER* instrument (Berger et al. 2010; Le Bouquin et al. 2011) in the H-band on several nights: 6–8 October 2014, 17–20 October 2014, 31 October–1 November 2014, 15–17 November 2014, 4–5 December 2014, 27–28 January 2015, and 5–6 February 2015. For all targets observed in 2014, we used the prism in low resolution (*SMALL*) which provides a spectral resolving power R∼15, the fringes being sampled over three spectral channels. Mid-December 2014, the detector of *PIONIER* was changed to the new *RAPID* detector, and therefore observations obtained in 2015 were obtained with the new observing mode, sampling the fringes over six spectral channels. The large *VLTI* configuration A1–G1–K0–J3 was used – except on the nights of 15–17 Nov. 2014 when A1–G1–I1–K0 was used and on 5–6 Feb. 2015 when H0–I1–D0–G1 was used – leading to baselines of 41 (H0-I1), 47 (G1-I1, H1-I1 and K0-I1), 56.8 (K0-J3), 64 (D0-H0), 71.7 (D0-G1 and H0-G1), 80 (A1-G1), 82.5 (D0-I1), 91 (G1-K0), 107 (A1-I1), 129 (A1-K0), 132.4 (G1-J3), and 140 metres (A1-J3).

Data reduction and calibration were done in the usual way with the `pndrs` package presented by Le Bouquin et al. (2011). Each pointing provides six visibilities and four closure phases dispersed over the few spectral channels across the H-band.

These interferometric observations were adjusted by a simple binary model. The diameters of the individual components, all smaller than 0.21 mas, are unresolved by our instrumental setup. The free parameters are thus the separation, the position angle of the secondary with respect to the primary, and the flux ratio. The different epochs were mostly adjusted independently. For few epochs, corresponding to small separations or incomplete dataset, the flux ratio was imposed following the results obtained at other epochs.

Fitting a binary model to interferometric observations is non-linear and non-convex[1]. We used a classical gridding approach to overcome these issues and to find the deepest minimum. We then used a Levenberg-Marquardt algorithm to determine the best-fit parameters and their covariance matrix. The astrometric error ellipsoid is the on-sky representation of this covariance matrix.

Our results are summarised in Table 1. The positions of the secondary component with respect to the primary are plotted on Fig. 1.

2.2 Verification and correction of the uncertainties

Reliable uncertainties are needed to derive masses from apparent positions and from RV measurements. This point is especially important hereafter, since several parameters in the common solution leading to the masses are coming as well from the interferometric observations as from the spectroscopic ones. This applies to the period P, the eccentricity e, the epoch of the periastron T_0 and the periastron longitude ω. Overestimating the uncertainties of the interferometric observations would lead to underestimate the weights of these observations and to exaggerate the contribution of the RV in the derivation of these terms, and vice versa.

To verify the uncertainties, the "visual" orbit of the

[1] Broadly speaking, a convex optimisation means that there is only one optimal solution, which is therefore globally optimal, i.e. a local minimum is a global one. This is not the case when adjusting a binary model to interferometric observations, as we need to cover the full range of parameters to determine the position of the global minimum.

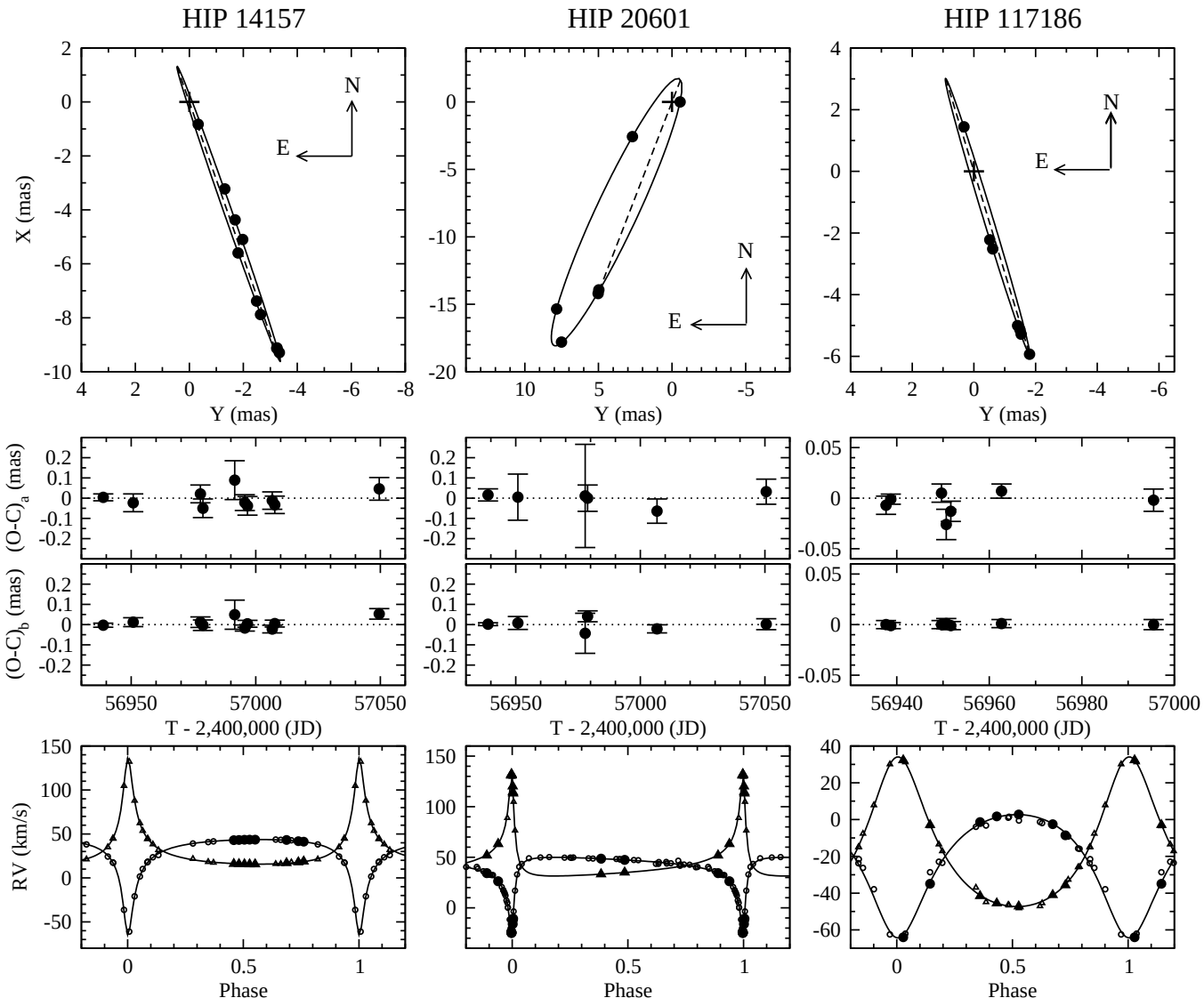

Figure 1. The combined orbits of the three SB2 observed with PIONIER. Upper row: the visual orbits; the node line is in dashes, while the position of the primary is indicated by the cross. Second row: the residuals along the semi-major axis of the error ellipsoid. Third row: the residuals along the semi-minor axis of the error ellipsoid. Last row: the spectroscopic orbits; the circles refer to the primary component, and the triangle to the secondary; the large filled symbols refer to the new RV measurements obtained with *HERMES* or *Sophie*. For each SB2, the RVs are shifted to the same zero point.

star is derived. Computing a visual orbit consists in searching seven unknowns: the period, P, the eccentricity, e, the epoch of the periastron, T_0, and the Thiele-Innes elements A, B, F, G. Therefore, a minimum of eight observations is needed to derive these terms and to estimate their errors. Since a relative position is a two-dimensional observation, this corresponds to four interferometric observations. For the least observed star, which is HIP 20601, we have six interferometric observations, resulting in five degrees of freedom in the derivation of the orbit. This is sufficient to allow the verification of the error estimations.

We derive the orbit of each binary, and we calculate F_2, the estimator of the goodness-of-fit defined in Stuart & Ord (1994):

$$F_2 = \left(\frac{9\nu}{2}\right)^{1/2}\left[\left(\frac{\chi^2}{\nu}\right)^{1/3} + \frac{2}{9\nu} - 1\right] \qquad (1)$$

where ν is the number of degrees of freedom and χ^2 is the weighted sum of the squares of the differences between the predicted and the observed values, normalised with respect to their uncertainties. When the predicted values are obtained through a linear model, F_2 follows the normal distribution $\mathcal{N}(0,1)$. When non–linear models are used, but when the errors are small in comparison to the measurements, as hereafter, the model is approximately linear around the solution, and F_2 follows also $\mathcal{N}(0,1)$. We also used simulations to verify that this property is true even when the number of degrees of freedom is as small as five.

It appears that, when the uncertainties provided by the

Table 1. The interferometric measurements. The column f_2/f_1 gives the flux ratio between the two components in the infrared H band. ρ is the separation between the components, and θ is the position angle of the secondary with respect to the primary component. σ_{max} and σ_{min} are the semi-major axis and the semi-minor axis of the error ellipsoid, respectively, corrected as indicated in section 2.2. The last column is the position angle of the semi-major axis of the error ellipsoid. The flux ratios flagged with asterisks were fixed in the fitting procedure.

HIP 14157						
MJD	f_2/f_1	ρ mas	θ deg	σ_{max} mas	σ_{min} mas	PA deg
56938.290	0.663	5.88	−162.05	0.017	0.010	132
56950.291	0.683	3.48	−157.77	0.044	0.022	118
56977.272	0.676	8.31	−161.43	0.044	0.026	155
56978.285	0.691	7.79	−161.28	0.046	0.026	159
56991.054	0.670*	0.89	−158.44	0.096	0.072	110
56995.109	0.688	4.69	−158.73	0.039	0.015	150
56996.165	0.676	5.47	−158.75	0.046	0.017	149
57006.115	0.662	9.68	−160.33	0.043	0.019	153
57007.140	0.664	9.87	−160.19	0.043	0.017	143
57049.045	0.666	9.69	−160.41	0.056	0.026	129
HIP 20601						
MJD	f_2/f_1	ρ mas	θ deg	σ_{max} mas	σ_{min} mas	PA deg
56938.367	0.402	3.72	+133.73	0.030	0.0067	139
56950.348	0.400*	0.55	−89.55	0.11	0.032	150
56977.353	0.400*	14.79	+160.44	0.25	0.099	148
56978.321	0.400*	15.06	+160.61	0.065	0.027	149
57006.187	0.402	19.32	+157.20	0.060	0.020	157
57050.051	0.387	17.24	+153.02	0.062	0.027	162
HIP 117186						
MJD	f_2/f_1	ρ mas	θ deg	σ_{max} mas	σ_{min} mas	PA deg
56937.179	0.440	2.28	−166.93	0.0090	0.0036	8
56938.210	0.440	2.59	−166.40	0.0045	0.0027	163
56949.162	0.434	5.20	−164.20	0.0086	0.0036	139
56950.187	0.437	5.35	−163.79	0.015	0.0050	134
56951.189	0.454	5.50	−163.84	0.0099	0.0036	141
56962.137	0.430	6.20	−163.09	0.0072	0.0036	141
56995.017	0.446	1.48	+12.55	0.011	0.0045	168

PIONIER reduction are taken into account, F_2 is systematically negative. This indicates that these uncertainties are overestimated. In order to keep the relative weights of the observations, the uncertainties of the positions of any star are divided by the same coefficient, in order to have $F_2 = 0$. The uncertainties σ_{min} and σ_{max} in Table 1 are thus obtained. It is worth noticing that they are similar to the errors expected for *Gaia* (Perryman 2005; Eyer et al. 2015).

3 THE RADIAL VELOCITIES AND THE SB2 ORBITS

3.1 Existing RV measurements

Radial velocity measurements are obtained from the SB9 Catalogue (Pourbaix et al. 2004), which is regularly updated and accessible on-line[2]. Primarily, the spectroscopic orbits of these stars were derived assigning weights to the measurements of the primary and of the secondary component. Since our purpose is to derive masses not only from these measurements, but also from new RV measurements and from interferometric observations, it is necessary to convert these weights to reliable uncertainties.

To evaluate the uncertainty of the RV of any component, the single-lined orbit of the star is derived. The weights of the RV measurements are transformed to uncertainties in order to get a SB1 orbit with $F_2 = 0$. It is worth noticing that this method is similar in its principle to the usual approach consisting in taking for the uncertainty the standard deviation of the residuals of the RV. However, it is much more reliable and it leads to uncertainties significantly larger.

When the RV uncertainties are obtained for both components, the SB2 orbit is derived, and F_2 is calculated again. A correction coefficient is applied to have at the end an SB2 orbit again with $F_2 = 0$. This method leads to the following results:

- For HIP 14157, the uncertainty of the RV measured by Fekel, Henry & Alston (2004) is 0.582 and 0.677 km s^{-1} for the primary and for the secondary component, respectively.
- The standard procedure requires an adaptation for the treatment of the RV measurements provided by Griffin et al. (1985) for HIP 20601. No weights are indicated by the authors, but 7 of the 63 measurements of the primary component are flagged as uncertain, and the secondary component received only 4 RV measurements. We assign 0.843 km s^{-1} to the uncertainty of the 56 "not uncertain" RV measurements, in order to get an SB1 orbit with $F_2 = 0$. The uncertainty of the "uncertain" primary RV is then 1.504 km s^{-1}, in order to still have $F_2 = 0$ for the SB1 orbit of the primary component. The uncertainty of the RV of the secondary component is then 3.000 km s^{-1}, in order to have $F_2 = 0$ for the SB2 orbit of the binary.
- For HIP 117186, the uncertainty of the RV measured by Nordström et al. (1997) is 1.837 and 1.487 km s^{-1} for the primary and for the secondary component, respectively.

The sets of RV of the three stars are further completed with high-accuracy measurements recently obtained.

3.2 New RV measurements

3.2.1 Radial velocities from the HERMES spectrograph

HIP 14157 received 8 RV measurements between January 2015 and August 2015. The fibre-fed *HERMES* spectrograph covers the whole wavelength range from 380 to 900 nm at a resolving power of $\sim 86,000$. A Python-based pipeline extracts a wavelength-calibrated and a cosmic-ray cleaned

[2] http://sb9.astro.ulb.ac.be/

spectrum. A restricted region, covering the range 478.11 – 653.56 nm (orders 55 – 74) was used to derive a cross-correlation function (CCF) with a spectral mask constructed from an Arcturus spectrum and containing 2103 useful spectral lines. A spectrum with a signal-to-noise ratio of 15 is usually sufficient to obtain a cross-correlation function (CCF) with a well-pronounced maximum.

Radial velocities are determined from a Gaussian fit to the core of the CCF with an internal precision of a few m s^{-1}. The most important external source of error is the varying atmospheric pressure in the spectrograph room (see Fig. 9 of Raskin et al. 2011), which is largely eliminated by the arc spectra taken for wavelength calibration. The long-term stability (years) of the resulting radial velocities is checked with RV standard stars from Udry, Mayor & Queloz (1999). Their standard-deviation distribution peaks at $\sigma_{RV} = 55$ m s^{-1}, which we adopt as the typical radial-velocity uncertainty for such relatively bright single stars. The RV standard stars have also been used to tie the *HERMES* RVs to the IAU standard system.

For a SB2 system, the reduction process leads to estimations of the uncertainties of the RV which are obviously underestimated, due to the pollution of the spectrum of each component by that of the other one. This appears clearly when the orbital elements are derived from the 8 *HERMES* observations of HIP 14157: the goodness-of-fit of the SB2 solution is as large as $F_2 = 17.3$, and the standard deviations of the residuals are 0.138 and 0.219 km s^{-1}, respectively. We assume then that the ratio of the true uncertainties is $\sigma_{RV2}/\sigma_{RV1} = 1.59$. The uncertainties are then increased, by adding quadratically a noise depending on the component, until we have $F_2 = 0$. This condition is fulfilled with the noises 0.187 and 0.298 km s^{-1}, respectively. This method is a bit different from the one applied above to derive the uncertainties of the previously published measurements, since the correction of the uncertainties is not done separately for each component. However, it is more suitable for an SB2 with few observations. The RVs of the components of HIP 14157 and the uncertainties thus obtained are listed in Table 3.

3.2.2 Derivation of RV from Sophie spectra with TODMOR

HIP 20601 and HIP 117186 received 12 and 7 *Sophie* spectra, respectively, between December 2010 and December 2014. The RV of the components are derived using the two-dimensional correlation algorithm *TODCOR* (Zucker & Mazeh 1994; Zucker et al. 2004), as explained hereafter.

The *TODCOR* algorithm calculates the cross-correlation of an SB2 spectrum and two best-matching stellar atmosphere models, one for each component of the observed binary system. This two-dimensional cross-correlation function (2D-CCF) is maximized at the radial velocities of both components. The multi-order version of *TODCOR*, named *TODMOR* (Zucker et al. 2004), determines the radial velocities of both components from the gathering of the 2D-CCF obtained from each order of the spectrum.

All *Sophie* multi-orders spectra are deblazed, then pseudo-continuum normalised using a p-percentile filter (Hodgson et al. 1985). The percentile p=0.5 selects the median among all flux values contained within the filter's window; any p>0.5 selects flux with value larger than the median. The percentile p and the width w of the filtering window are chosen so that the resulting normalised spectra are as flat as possible, while not altering the depth and shape of any lines. These constraints led us to chose for both targets w∼1,300 pixels (∼33Å); the width of one *Sophie* order is about 4,000 pixels (∼100Å); 33Å is about twice the full width at half-maximum for a Balmer line of early-type stars and for Ca II lines of late-type stars. The value of p was determined independently for each order by maximising the two dimensional cross-correlation.

We determined for the two components of each binary best-matching atmospheric models from the *PHOENIX* library (Husser et al. 2013). For consistency, we also applied a p-percentile filter on the spectra of the models, with p=0.99 and the same window's width as for HIP 117186 and HIP 20601 spectra, of ∼1,300 pixels. On those spectra for which both peaks of the SB2 components are well separated, we optimized the two-dimensional cross-correlation function varying the effective temperature, the stellar rotation's $v \sin i_r$, the metallicity and the surface gravity's $\log g$ of both components.

The grid for optimisation is defined with $T_{\rm eff}$ extending from 3,000 to 6,900 K with steps of 100 K and from 7,000 to 11,000 with steps of 200 K; $\log(g)$ extending from 2 to 6 dex with steps of 0.5 and linearly interpolated from 4 to 5.5 with steps of 0.1; [Fe/H] extending from −1.5 to 1 dex with steps of 0.5 and linearly interpolated from −1 to 0.5 with steps of 0.1; $v \sin i_r$ extending continuously from 0 to 200 km.s^{-1}; and the flux ratio, α, extending continuously from 0 to 1. The secondary $\log g$ was fixed for each set of test parameters with respect to primary and secondary effective temperatures, primary $\log g$ and estimated mass ratio q=M_2/M_1, using the following relation

$$\begin{aligned} \log g_2 - \log g_1 &= \log q + 2 \log \frac{R_2}{R_1} \\ &= \log q + \log \alpha - \log \frac{B(T_{\rm eff,2}, \lambda_{med,20})}{B(T_{\rm eff,1}, \lambda_{med,20})} \end{aligned} \quad (2)$$

where $B(T_{\rm eff})$ is the value of the blackbody flux for effective temperature $T_{\rm eff}$ at the median wavelength $\lambda_{med,20}$ of *Sophie*'s median order n°19 over 39.

The derived values of the stellar parameters are given for both components in Table 2. For HIP 117186 only one spectrum had large enough separation between the primary and secondary peaks, namely the spectrum observed at periastron passage. For HIP 20601, all spectra gave very consistent results, up to 5K and 100K in effective temperature for the primary and secondary respectively, 0.03 and 0.4 in $\log g$, 0.2 and 0.6 km s^{-1} in v $\sin i_r$, 0.01 in metallicity, and 0.01 in flux ratio. However, the individual uncertainties are much larger than these scatter values, so we give here the average individual uncertainties divided by the square-root of the number of spectra used for deriving the parameters, namely $\sqrt{N_{\rm spec}}$.

The individual uncertainties were determined by defining as lower and upper bounds the values of the parameters at maximum of the CCF minus the estimated level of the noise in the CCF. This level is given by $\sigma_{\rm CCF} \sim \sqrt{\langle 1/{\rm SNR}^2 \rangle} / \|F\|$, the order-average noise-to-signal

Table 2. The stellar parameters determined by optimisation of the two-dimensional cross-correlation function obtained with *TODMOR*. At the bottom, $N_{\rm spec}$ is the number of spectra used to derive the parameters values.

Parameters	HIP 20601	HIP 117186
$T_{\rm eff,1}$[K]	5600±90	6580±230
$\log g_1$[dex]	4.43±0.26	3.8±0.6
$v_1 \sin i_{r\ 1}$[kms^{-1}]	4.6±1.0	43±13
$T_{\rm eff,2}$[K]	4550±550	6550±490
$\log g_2$[dex]	4.76±0.92	4.32±0.82
$v_2 \sin i_{r\ 2}$[kms^{-1}]	<2	13±11
m/H[dex]	-0.38±0.10	-0.35±0.24
α [flux ratio]	0.106±0.006	0.374±0.151
$N_{\rm spec}$	4	1

ratio in the normalised spectrum F divided by its norm over all orders

$$\langle 1/{\rm SNR}^2 \rangle = \frac{1}{N_{orders}} \times \sum_{i \in {\rm orders}} \left(\frac{1}{{\rm SNR}_i} \right)^2 \qquad (3)$$

$$\|F\| = \sqrt{\sum_{i \in {\rm orders}} \sum_{p \in {\rm pixels}} F_{i,p}^2} \qquad (4)$$

Finally, we applied *TODCOR* to all multi-order spectra of each target and determined the radial velocities of both components. We discarded several orders of the spectra of HIP 20601 and HIP 117186, which were strongly affected by telluric lines (orders n°31, 34, 36 and 39). At a given exposure, for each of the selected orders, we calculated a two dimensional cross-correlation function, from which we derived the maximising values of radial velocities for the primary and the secondary.

For each target, there are systematic order-to-order variations of the radial velocity measurements, different for each SB2 component. These systematics come from signal-to-noise, number of atomic lines available, and discrepancies of the models with the real spectrum; they are specific to each component and each order. To estimate them, we first calculated for each exposure the residuals of the velocities derived for all individual order around the median velocity; then we considered the residuals obtained for all exposures at an individual order, and calculated the systematic shift for this order as the median of the residuals. We estimated as well a measurement error for each order from the scatter of its residuals about the systematics.

Then, we determined at all epochs the radial velocities of the primary and the secondary and their uncertainties from the weighted average and the square-root of the weighted variance of the corrected order-by-order velocities.

The uncertainties of the RV measurements thus obtained need to be verified, and possibly corrected, since the method of calculation leads to overestimating the errors. Again, the verification is based on F_2, and when a correction is necessary, it is done in order to obtain $F_2 = 0$. For HIP 20601, we have 12 RV measurements for each component. We derive the 6 parameters of each SB1 orbit, and F_2 is obtained with 6 degrees of freedom. For the primary and for the secondary component, we obtain $F_2 = -1.63$ and -2.43, respectively. These small values clearly confirm that the uncertainties are too large for both components. They are multiplied by 0.554 and 0.369, respectively, in order to have $F_2 = 0$. When the SB2 orbit is derived with the corrected uncertainties, $F_2 = 0.32$. Although this value seems quite acceptable, we apply an additional correction factor of 1.058, in order to have $F_2 = 0$ for the SB2 orbit coming from our measurements, as we did for the SB2 orbit obtained from previously published measurements, in section 3.1.

We have only 7 RV measurements for each component of HIP 117186. This number is sufficient to derive the SB1 orbits, but, with only one degree of freedom, the method applied to HIP 20601 is not sufficiently robust to lead to reliable uncertainties. Therefore, we consider only the SB2 orbit, which is derived with 6 degrees of freedom. We have

Table 3. The new RVs obtained from *HERMES* (HIP 14157) or from *Sophie* (HIP 20601 and HIP 117186). The uncertainties are revised as explained in the text.

HIP 14157

BJD −2400000	RV_1 km s^{-1}	$\sigma_{RV\ 1}$ km s^{-1}	RV_2 km s^{-1}	$\sigma_{RV\ 2}$ km s^{-1}
56672.3674	43.525	0.189	17.222	0.300
57052.4032	43.272	0.189	16.272	0.301
57053.3496	43.454	0.189	16.047	0.300
57054.3817	43.694	0.188	15.918	0.300
57055.3393	43.869	0.189	15.790	0.300
57056.3651	43.881	0.189	15.774	0.300
57237.7366	42.125	0.188	18.107	0.300
57238.7311	41.513	0.189	18.983	0.301

HIP 20601

BJD −2400000	RV_1 km s^{-1}	$\sigma_{RV\ 1}$ km s^{-1}	RV_2 km s^{-1}	$\sigma_{RV\ 2}$ km s^{-1}
55532.4785	25.8044	0.0423	62.9854	0.1795
56243.5140	46.9337	0.0176	34.5268	0.2933
56323.2404	-24.2847	0.0196	130.7605	0.1366
56323.3136	-24.7068	0.0185	131.1920	0.1084
56323.3628	-24.9163	0.0198	131.5768	0.1179
56323.4538	-25.1587	0.0193	131.8981	0.1920
56323.5102	-25.2156	0.0224	132.0942	0.1792
56324.2438	-16.4490	0.0251	119.8076	0.1136
56324.4318	-12.0964	0.0125	114.1730	0.1463
56324.4718	-11.1097	0.0199	112.7543	0.2391
56619.5265	33.7880	0.0315	52.4828	0.3178
57009.4242	48.1646	0.0224	33.0725	0.2846

HIP 117186

BJD −2400000	RV_1 km s^{-1}	$\sigma_{RV\ 1}$ km s^{-1}	RV_2 km s^{-1}	$\sigma_{RV\ 2}$ km s^{-1}
55864.3650	-8.5826	0.8246	-35.8419	0.2292
56147.5270	-64.0310	0.8484	32.1576	0.1751
56243.3282	-34.8861	1.4155	-3.0639	0.2020
56525.5154	1.6961	0.4467	-45.6927	0.1320
56619.4355	2.7450	0.7522	-47.3041	0.1390
56889.5626	-2.5384	0.7092	-41.1859	0.1439
56948.4278	-1.3476	0.7158	-41.6893	0.1622

$F_2 = -0.81$, and we correct the uncertainties by multiplying them by 0.766. After this correction, we verify that both SB1 orbits have acceptable values of F_2: we find $F_2 = -0.13$ and -0.77, respectively.

The RVs and the uncertainties finally derived are in Table 3.

3.3 The SB2 orbits

We compute the SB2 orbits, taking into account simultaneously the existing and the new measurements. In addition to the usual parameters of an SB2 orbit, we introduce 3 offsets of the RV measurements: d_{n-p}, the offset between the new measurements and the published ones, and d^p_{2-1} and d^n_{2-1}, the offsets between the RV of the secondary components and the RV of the primary components, for the published and for the new measurements. The systemic velocity, V_0, is derived in the system of the new RV measurements of the primary component.

For HIP 14157 and HIP 20601, $F_2 = -0.041$ and -0.16, respectively, indicating that both sets of measurements are quite compatible. For HIP 117186, $F_2 = 0.78$, since some discrepancies appear between the SB2 orbit derived from the new measurements and the preceding one; the most important is the mass ratio, which is 0.771 ± 0.021 with the previously published measurements and 0.844 ± 0.012 with our observations. Nevertheless, the SB2 orbit obtained from both sets of RVs is basically indistinguishable from the one derived from our measurements alone, but the period is much more accurate, thanks to the extension of the timespan covered by the observations. The new SB2 orbits are presented in Table 4.

4 THE MASSES

4.1 Derivation of the masses

The masses of the components are directly derived from the interferometric and from the RV measurements, taken into account simultaneously. However, we increase the RV uncertainties of HIP 117186 by 1.088, which would lead to a SB2 orbit with $F_2 = 0$. This operation increases the relative weights of the interferometric measurements in the derivation of the combined orbit. The solution consists in up to 13 independent parameters, which are: the orbital parameters P, T_0, e, V_0, ω_1, i, Ω_1, the masses $\mathcal{M}_1$, $\mathcal{M}_2$, the trigonometric parallax ϖ, and also the RV offsets d_{n-p}, d^p_{2-1} and d^n_{2-1}. It is worth noticing that we prefer to directly obtain $\mathcal{M}_1$, $\mathcal{M}_2$ and ϖ, rather than the observational parameters K_1, K_2 and a, the apparent semi-major axis of the interferometric orbit. The advantage of this method is that it leads directly to the uncertainties of the masses and of the parallax, in place of the uncertainties on K_1, K_2 and a when the latter parameters are obtained from the combined interferometric and spectroscopic observations. The parameters of the combined solutions are presented in Table 5. The uncertainties of masses range between 0.0019 and 0.034 $\mathcal{M}_\odot$, and the relative errors range between 0.26 and 2.4 %. This is similar to the accuracies expected using the Gaia astrometry.

Table 5. The combined VB+SB2 solutions; For consistency with the SB orbits and with the forthcoming astrometric orbit, ω and Ω both refer to the motion of the primary component.

	HIP 14157	HIP 20601	HIP 117186
P (days)	43.32032	156.38020	85.8238
	± 0.00013	± 0.00026	± 0.0012
T_0 (BJD-2400000)	51487.5005	56636.6713	56402.576
	± 0.0079	± 0.0027	± 0.072
e	0.7594	0.85148	0.32702
	± 0.0010	± 0.00025	± 0.00068
V_0 (km s^{-1})	30.743	41.623	-19.89
	± 0.091	± 0.014	± 0.33
ω_1 (^{o})	174.69	202.026	176.07
	± 0.17	± 0.086	± 0.32
Ω_1(^{o}; eq. 2000)	19.141	340.526	16.928
	± 0.082	± 0.058	± 0.047
i (^{o})	92.24	103.138	88.054
	± 0.18	± 0.077	± 0.043
a^a (mas)	5.810	11.339	4.677
	± 0.034	± 0.068	± 0.032
$\mathcal{M}_1$ ($\mathcal{M}_\odot$)	0.982	0.9808	1.686
	± 0.010	± 0.0040	± 0.021
$\mathcal{M}_2$ ($\mathcal{M}_\odot$)	0.8819	0.7269	1.390
	± 0.0089	± 0.0019	± 0.034
ϖ (mas)	19.557	16.702	8.445
	± 0.078	± 0.037	± 0.075
$n_{VLTI} \times 2$	20	12	14
$\sigma_{(o-c)\ VLTI}$ (mas)	0.035	0.031	0.0084
n_{RV1}	23+8	63+12	19+7
$\sigma_{(o-c)\ RV1}$ (km s^{-1})	0.562, 0.156	0.952, 0.015	2.40, 0.89
n_{RV2}	23+8	4+12	19+7
$\sigma_{(o-c)\ RV2}$ (km s^{-1})	0.646, 0.282	2.54, 0.143	1.11, 0.23
d_{n-p} (km s^{-1})	0.323	-0.441	0.822
	± 0.172	± 0.111	± 0.563
d^p_{2-1} (km s^{-1})	0.408	0.436	0.549
	± 0.198	± 1.513	± 0.606
d^n_{2-1} (km s^{-1})	-0.149	0.077	-0.184
	± 0.161	± 0.135	± 0.335

[a] the uncertainty refers to the VB solution

4.2 Notes on individual objects

HIP 14157. This system is extensively discussed by Fekel, Henry & Alston (2004), who pointed out that the primary is a BY Dra variable star with a variability amplitude around 0.02 mag. Due to an inclination almost edge-on, the masses of the components are close to the minimum masses that they found. We confirm then that the mass of the K2-K3 V secondary component is 0.882 $\mathcal{M}_\odot$. This is larger than the canonical value, which is between 0.67 $\mathcal{M}_\odot$ (for a K5 V star), and 0.79 $\mathcal{M}_\odot$ (for a K0 V star) according to Cox (2000). Such discrepancy is not surprising, but known since a while, since Griffin et al. (1985) and references therein already pointed out that the real masses of K-type stars are usually 15 % larger than the canonical values. In a similar way, we find that the primary component is too heavy for a K0 V star. The minimum projected separation between the components is only 0.090 mas, corresponding to 0.99 solar radius. Since Fekel et al. estimated the stellar radii $R_1 = 0.99\ \mathcal{R}_\odot$ and $R_2 = 0.76\ \mathcal{R}_\odot$, the system is very likely an eclipsing one.

Table 4. The orbital elements of the three stars, derived from both the previously existing RV measurements and from the new ones. The minimum masses and minimum semi-major axes are derived from the true period ($P_{true} = P \times (1 - V_0/c)$).

HIP	P	T_0(BJD)	e	V_0	ω_1	K_1	$\mathcal{M}_1 \sin^3 i$	$a_1 \sin i$	N_1	d_{n-p}	$\sigma(O_1 - C_1)_{p,n}$
						K_2	$\mathcal{M}_2 \sin^3 i$	$a_2 \sin i$	N_2	d^p_{2-1}, d^n_{2-1}	$\sigma(O_2 - C_2)_{p,n}$
	(d)	2400000+		(km s^{-1})	(°)	(km s^{-1})	($\mathcal{M}_\odot$)	(Gm)		(km s^{-1})	(km s^{-1})
14157	43.32058	51487.495	0.7602	30.751	174.60	54.31	0.980	21.014	23+8	0.343	0.555,0.142
	±0.00049	±0.012	±0.0015	±0.094	±0.22	±0.29	±0.010	±0.094		±0.176	
						60.45	0.8801	23.39	23+8	0.434, -0.167	0.636,0.312
						±0.34	±0.0089	±0.11		±0.201, ±0.170	
20601	156.38019	56636.6716	0.85147	41.623	202.042	37.342	0.9060	42.101	63+12	-0.442	0.951,0.015
	±0.00027	±0.0027	±0.00025	±0.014	±0.089	±0.017	±0.0037	±0.025		±0.112	
						50.390	0.6714	56.81	4+12	0.416, 0.071	2.53,0.143
						±0.088	±0.0018	±0.10		±1.531, ±0.136	
117186	85.8266	56403.36	0.3362	-19.59	178.75	33.40	1.627	37.12	19+7	1.121	2.14,0.799
	±0.0017	±0.27	±0.0035	±0.32	±0.86	±0.39	±0.028	±0.44		±0.527	
						40.31	1.348	44.81	19+7	0.519, -0.967	1.41,0.107
						±0.18	±0.033	±0.23		±0.558, ±0.411	

Table 6. The magnitudes in the infrared H band, and the absolute magnitudes of the components derived from the flux ratios taken from Table 1 and from the parallaxes in Table 5.

	HIP 14157	HIP 20601	HIP 117186
H_{tot}	6.629 ± 0.029	7.209 ± 0.047	6.252 ± 0.031
ΔH	0.429 ± 0.017	0.999 ± 0.016	0.891 ± 0.020
$M_{H\,1}$	3.645 ± 0.031	3.687 ± 0.047	1.281 ± 0.037
$M_{H\,2}$	4.073 ± 0.032	4.686 ± 0.049	2.172 ± 0.039

HIP 20601. The star is a candidate member of the Hyades cluster (Perryman et al. 1998; de Bruijne, Hoogerwerf & de Zeeuw 2001). Griffin et al. (1985) estimated that the spectral types of the components are probably G6 and K5, in good agreement with our estimates of the effective temperatures. As a consequence, the masses are around 7 % larger than the canonical values listed in Cox (2000).

HIP 117186. The effective temperatures of the components correspond to spectral types around F5, and the canonical masses are around 1.4. This corresponds well to the mass of the secondary component, but is around 20% percent less than the mass of the primary component.

5 THE INFRARED MASS-LUMINOSITY RELATION

The data derived from *PIONIER* observations include the flux ratios f_2/f_1 which are listed in Table 1. The photometric band is similar to the infrared H band of 2MASS (Skrutskie et al. 2006), and, for each binary, we derive the mean value of the magnitude difference, ΔH, and its standard error. The total H magnitudes of the binaries are taken from Cutri et al. (2003), and the individual absolute H magnitude of the components are then computed, using the parallaxes from Table 5. The results are given in Table 6.

The masses and the absolute H magnitudes of the six components are plotted on a mass-luminosity diagram in Fig. 2. The mass-luminosity relation of Henry & McCarthy (1993) is also shown for comparison. Although the masses of our stars are within the uncertainties of the canonical relation, they are in excess by around 8 % when H_{abs} is between 3.6 and 4.7 mag.

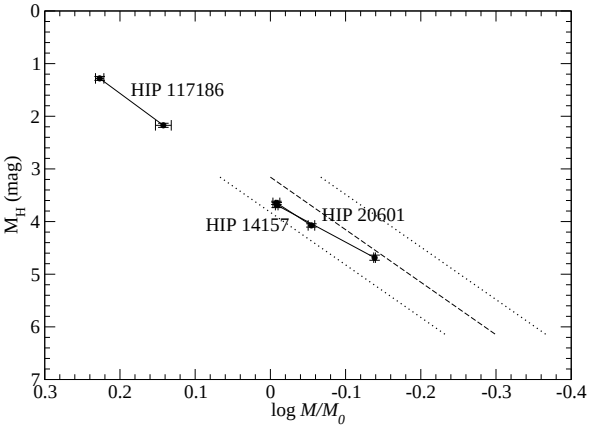

Figure 2. The mass-luminosity diagram in the infrared H band. The relation of Henry and McCarthy is in dashes, with limits in dotted lines.

Table 7. The *Hipparcos 2* parallaxes, before and after taking into account the orbital motion (ϖ_{SS} and ϖ_{AO}, respectively). a_0 is the semi-major axis of the photocentric orbit derived from *Hipparcos* data.

	HIP 14157	HIP 20601	HIP 117186
ϖ_{SS} (mas)	19.78 ± 1.10	15.20 ± 1.35	6.94 ± 0.57
$F_{2\,SS}$	0.69	-0.21	2.24
ϖ_{AO} (mas)	19.10 ± 1.09	14.84 ± 1.41	7.93 ± 0.64
a_0 (mas)	3.06 ± 1.54	2.45 ± 1.40	1.07 ± 0.48
$F_{2\,AO}$	0.399	-0.42	2.03

6 VERIFICATION OF THE *HIPPARCOS* PARALLAXES

The elements of the combined solutions presented in Table 5 include parallaxes with errors between 0.037 and 0.078 mas.

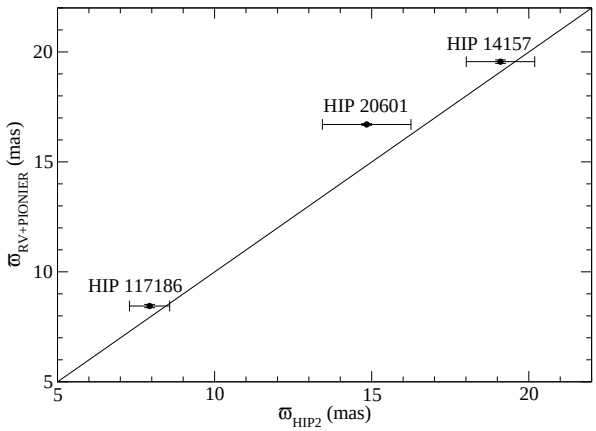

Figure 3. Comparison of the parallaxes derived in the combined solution with the Hipparcos 2 parallaxes corrected for the orbital motion.

They are roughly 10 times better than the errors of the parallaxes coming from *Hipparcos*. However, in the *Hipparcos 2* catalogue, the parallaxes of these stars were derived through the single-star (SS) model, ignoring that they are binaries. As a consequence, a discrepancy between our parallaxes and the *Hipparcos* ones could be due to a reduction based on the use of the single–star model, and not to errors in the *Hipparcos* transits. In order to check the reliability of *Hipparcos* itself, we first computed the corrections of the *Hipparcos 2* parallaxes. For that purpose, the residuals of any single–star solution were input in the computation of an astrometric orbital (AO) solution. However, except for the astrometric semi-major axis, a_0, all the orbital elements were fixed on the values already obtained. The new parallaxes, ϖ_{AO}, are listed in Table 7, with a_0 and the goodness-of-fit of the new solution, $F_{2\,AO}$. The uncorrected parallax and the related goodness-of-fit, $F_{2\,SS}$, are indicated for comparison. F_2 is always ameliorated when the orbital motion is taken into account, and a_0 is always smaller than twice its uncertainty. Therefore, it would not have been not possible to detect the orbital motion from *Hipparcos* alone.

The corrected *Hipparcos* parallaxes are compared to our parallaxes in Fig. 3. For HIP 14157 and HIP 117186, the agreement is less than the standard error. For HIP 20601, the difference is (1.86 ± 1.41) mas, ie 1.3 times the standard error. This is still a rather good agreement, and it seems that the discrepancy found by Fekel for HD 207651 is due to peculiarities, such as the presence of a third star.

7 CONCLUSION

We have combined interferometric observations performed with the *VLTI* with radial velocities in order to derive the masses of the components of three binary stars. Thanks to the exquisite accuracy of the *PIONIER* observations, but also to the fact that the orbits are all close to edge-on, the accuracy of the masses thus obtained is between 0.26 and 2.4 %. This is less than the 3 % limit applied by Torres, Andersen & Giménez (2010) when they set up their list of accurate masses. This is also close to the uncertainties that we expect to obtain combining the RV measurements with *Gaia* astrometry.

Five of the six masses are a few percent larger than the expectations coming from the standard spectral type–mass calibration, confirming Griffin et al. (1985). The masses below one solar mass are also around 8 % larger than the masses derived from the mass-luminosity relation of Henry & McCarthy (1993), although they are within their error interval. One of our star (HIP 14157) should be observed as an eclipsing binary; this would confirm the small inclination that we have found, and therefore improve the accuracy of the masses, but it would also make possible the estimation of the radii of the components.

The parallaxes are derived in the same time as the orbital elements of the binaries, with an accuracy much better than that of the *Hipparcos 2* catalogue. The reliability of the Hipparcos parallaxes is confirmed.

ACKNOWLEDGMENTS

This project was supported by the french INSU-CNRS "Programme National de Physique Stellaire" and "Action Spécifique *Gaia*". *PIONIER* is funded by the Université Joseph Fourier (UJF), the Institut de Planétologie et d'Astrophysique de Grenoble (IPAG), and the Agence Nationale pour la Recherche (ANR-06-BLAN-0421, ANR-10-BLAN-0505, ANR-10-LABX56). The integrated optics beam combiner is the result of a collaboration between IPAG and CEA-LETI based on CNES R&T funding. The *HERMES* spectrograph is supported by the Fund for Scientific Research of Flanders (FWO), the Research Council of K.U.Leuven, the Fonds National de la Recherche Scientifique (F.R.S.-FNRS), Belgium, the Royal Observatory of Belgium, the Observatoire de Genève, Switzerland and the Thüringer Landessternwarte Tautenburg, Germany. We are grateful to the staff of the Haute–Provence Observatory, and especially to Dr F. Bouchy, Dr H. Le Coroller, Dr M. Véron, and the night assistants, for their kind assistance. We warmly thank Dr. C. Soubiran for her helpful advices. This research has received funding from the European Community's Seventh Framework Programme (FP7/2007-2013) under grant-agreement numbers 291352 (ERC). This work made use of the Smithsonian/NASA Astrophysics Data System (ADS) and of the Centre de Donnees astronomiques de Strasbourg (CDS).

REFERENCES

Berger J.P. et al., 2010, Proc. SPIE7734, Optical and Infrared Interferometry II, 7734, 35
Cox A.N., 2000, Allen's Astrophysical Quantities, 4th ed., New York: AIP Press; Springer
Cutri R.M. et al., 2003, 2Mass All Sky Catalog of point sources, Vizier Online Data Catalogue 2246,0
de Bruijne J. H. J., Hoogerwerf R., de Zeeuw, P. T., 2001, A&A, 367, 111
ESA, 1997, The Hipparcos and Tycho Catalogues, SP-1200
Eyer L. et al., 2015, in Rucinski S.M., Torres G., Zejda M., eds, ASP Conf. Ser. Vol.496, Living Together: Planets, Host Stars and Binaries. Astron. Soc. Pac., San Francisco, p. 121
Fekel F., 2015, AJ 149, 83

Fekel F., Henry G., Alston F., 2004, AJ, 127,2303
Griffin R.F., Gunn J.E., Zimmerman B.A., Griffin R.E.M., 1985, AJ 90, 609
Halbwachs J.L. et al., 2014, MNRAS 445, 2371
Henry T.J., McCarthy D.W., 1993, AJ 106, 773
Husser T.-O. et al., 2013, A&A, 553, A6
Hodgson R.M., Bailey D.G., Naylor M.J., Ng A.L.M., McNeil S.J., 1985, Image Vision Comput., 3(1), 4-14
Le Bouquin J.B. et al., 2011, A&A 535, 67L
Mora A. et al., 2015, arXiv150302614
Nordström B., Stefanik R. P., Latham D. W., Andersen J., 1997 A&AS 126, 21
Perryman M.A.C., 2005, in The Three-Dimensional Universe with *Gaia*, ESA SP-576, pg 15
Perryman M.A.C. et al., 1998, A&A 331, 81
Pourbaix D. et al., 2004, A&A 424, 727
Raskin G. et al., 2011, A&A 526, A69
Skrutskie M.F. et al., 2006, AJ 131, 1163
Stuart A., Ord K., 1994, Kendall's Advanced Theory of Statistics, vol. 1. Edward Arnold, London
Torres G., Andersen J., Giménez A., 2010, Astron. Astrophys. Rev., 18, 67
Udry S., Mayor M., Queloz D, 1999, in Hearnshaw J.B., Scarfe C.D., eds, Proc. IAU Coll. 170, Precise Stellar Radial Velocities. Astron. Soc. Pac., San Francisco, p. 210 p. 367
van Leeuwen F., 2007, A&A 474, 653
Zucker S., Mazeh T., 1994, ApJ, 420, 806
Zucker S., Mazeh T., Santos N. C., Udry S., Mayor M., 2004, A&A, 426, 695

This paper has been typeset from a TEX/ LATEX file prepared by the author.